SCIENTIFIC REPORTS

OPEN

SUBJECT AREAS:
TWO-DIMENSIONAL MATERIALS
NANOSCALE DEVICES

Received
11 August 2014

Accepted
29 October 2014

Published
26 November 2014

Correspondence and requests for materials should be addressed to C.-Y.X. (cy_xu@hit.edu.cn) or L.Z. (lzhen@hit.edu.cn)

Photodiode-Like Behavior and Excellent Photoresponse of Vertical Si/Monolayer MoS_2 Heterostructures

Yang Li[1], Cheng-Yan Xu[1,2], Jia-Ying Wang[1] & Liang Zhen[1,2]

[1]School of Materials Science and Engineering, Harbin Institute of Technology, Harbin 150001, China, [2]MOE Key Laboratory of Micro-systems and Micro-structures Manufacturing, Harbin Institute of Technology, Harbin 150080, China.

Monolayer transition metal dichalcogenides (TMDs) and their van der Waals heterostructures have been experimentally and theoretically demonstrated as potential candidates for photovoltaic and optoelectronic devices due to the suitable bandgap and excellent light absorption. In this work, we report the observation of photodiode behavior in (both *n*- and *p*- type) silicon/monolayer MoS_2 vertical heterostructures. The photocurrent and photoresponsivity of heterostructures photodiodes were dependent both on the incident light wavelength and power density, and the highest photoresponsivity of 7.2 A/W was achieved in *n*-Si/monolayer MoS_2 vertical heterostructures photodiodes. Compared with *n*-Si/MoS_2 heterostructures, the photoresponsivity of *p*-Si/MoS_2 heterostructure was much lower. Kelvin probe microscope (KFM) results demonstrated the more efficient separation of photogenerated excitons in *n*-Si/MoS_2 than that in *p*-Si/MoS_2. Coupling KFM results with band alignments of (*p*-, *n*-) Si/MoS_2 heterostructures, the origins of photodiode-like phenomena of *p*-Si/MoS_2 and *n*-Si/MoS_2 have been unveiled, that is intrinsic built-in electric field in p-n junction, and modulated barrier height and width at the interface in n-n junction. Our work may benefit to the deep understanding of the integration of two-dimensional materials with more conventional three-dimensional semiconductors, and then contribute to the developments in the area of van der Waals heterostructures.

Two-dimensional transition metal dichalcogenides (TMDs) have been experiencing significant progress because of the wide range of physical and chemical properties from the ultrathin planar structures at the atomic scale, such as strong electron-hole confinement, and excellent mechanical and thermal stability[1–4]. Besides, due to the relatively small bandgap, TMDs are also considered as excellent light absorbers, stimulating the development of TMDs-based photovoltaic and optoelectronic devices recently[5,6]. Molybdenum disulfide (MoS_2), a typical member of TMDs, is demonstrated as a promising candidate that goes beyond graphene for next generation of optoelectronics and spintronics due to the intrinsic and tunable bandgap, relatively high carrier mobility, and strong coupling of spin and valley degrees[7–9]. In the past few years, more researches concentrated on pursuing better photoresponsivity and broad wavelength response of MoS_2-based photodetectors[10–14]. For example, Yin *et al.* first fabricated monolayer MoS_2 phototransistor with higher responsivity (7.5 mA/W) than that of graphene[10]. The wavelength-dependent photosensivity of monolayer to trilayer MoS_2 field-effect transistors was investigated by Im *et al.*, and the results revealed that monolayer and bilayer MoS_2 exhibited excellent photodetection capabilities for green light, while tri-layer MoS_2 was efficient for red light detection[12]. By optimizing the carrier mobility, electrical contact quality and positioning technique, the maximum external photoresponsivity of 880 A/W was achieved for mechanically exfoliated monolayer MoS_2[13]. To further improve the optoelectronic property for potential photodetection or photovoltaic applications, TMDs based heterostructures have emerged, and gained much attention in recent years[15–22]. MoS_2/graphene, MoS_2/WS_2 and MoS_2/CNT heterostructures have been demonstrated to achieve the superior light absorption and photovoltaic effects theoretically and experimentally, where the built-in electric field at the interface leads to the separation of photo-excited carriers. Very recently, light-emitting diodes and solar cells based on monolayer MoS_2/*p*-Si heterojunctions were realized, and the external quantum efficiency of solar cells based on MoS_2/*p*-Si exceeded 60%[23,24]. However, the photodiodes behavior of MoS_2 based heterostructures and their applications to photodetection have not been fully studied until now.

In this work, we study the photodiode behavior of (*n* and *p*-type) Si/MoS_2 vertical heterostructures under illumination with different light wavelengths and power densities, and then discuss the feasibility to detect the

wavelength-dependent light by reverse photocurrent measurement. In addition to *p*-Si/MoS_2 (p-n junction), where the photodiode behavior was resulted from the intrinsic built-in electric field at the interface of p-n junction, the abnormal photodiode-like behavior for *n*-Si/MoS_2 heterostructures was also uncovered, which was attributed to the built-in electric field from modulated barrier height (and width) induced by the photogenerated excitons in the vicinity of the interface. The strong electric field at the interface and the short carrier diffusion path lead to the high photoresponsivity, approaching to about 7.2 A/W for *n*-Si/monolayer MoS_2 heterostructures.

Results

Monolayer MoS_2 was mechanically exfoliated, and then transferred to *p*- and *n*-type silicon substrates by using transfer methods described in ref. 25. Upon locating the position of monolayer MoS_2 using atomic force microscopy (AFM) and Raman spectra (Figure S1, SI), Ag electrode with thickness of 60 nm was deposited close to MoS_2 flake with the help of shadow mask. Note that the contrast of monolayer MoS_2 on Si substrates is very weak, it should be serious to verify it by AFM and Raman spectra. Ag was chosen as the electrode due to the lower contact resistance between Ag and Si. The *I*–*V* curve of Ag/Si contacts presented nearly perfect linear characteristics, as shown in Supporting Information (Figure S2, SI). The electrical property measurement was conducted by conductive atomic force microscope (C-AFM, Bruker Dimension ICON-Pt) equipped with illumination system. Co/Cr tips were chosen due to the high abrasion resistance (See Figure S3, SI) and lower work function to match the band alignment of monolayer MoS_2, and to assure the Ohmic contact between the tip and monolayer MoS_2. Local *I*–*V* curves were obtained by positioning the tip directly at selected areas and applying a bias between the tip and substrate while measuring the current by recording the response of the built-in current preamplifier. The schematic illustration of the experimental procedures was depicted in Figure 1a. In these junctions, the excitons were generated in both monolayer MoS_2 and Si, and then separated by the built-in electric field at the interface, leading to the photodiodes-like behaviors as following.

It should be noted that the stability of *I*–*V* curves depends on the roughness of samples as well as the tip-sample contact force for C-AFM measurements[26,27]. During our experiments, the silicon substrates were very smooth with roughness of less than 0.1 nm. Therefore, we only concerned the effect of contact force on the electrical properties measurement. As shown in Figure 1b, when the contact force was about 2 nN, the *I*–*V* curves vibrated inhomogeneously, indicating the non-ideal contact between the tip and sample. By increasing the contact force from 7 to 11.5 nN, the reverse bias presented negligible variation and the curves did not modulate with contact force, indicating the suitable contact at the interface. However, the reverse bias increased rapidly when the contact force approached to 20 nN or larger (inset of Figure 1b), which may be attributed to the plastic deformation of monolayer MoS_2, destroying the contact interface[28,29]. Therefore, in order to avoid the severe deformation of MoS_2, mitigate the wear of tips and improve the reproducibility of *I*–*V* curves, the contact force between the tip and samples maintained to be 9 nN in our C-AFM tests.

Next, we explicitly analyzed the dependence of photoreponse behavior of *n*-Si/monolayer MoS_2 heterostructures on light wavelength and power density. Figure 2a–d presents *I*–*V* curves of *n*-Si/MoS_2 heterostructures with light illumination of 365, 450, 550 and 650 nm, respectively. Before illumination, the heterostructures presented perfect rectification characteristics, namely, where the reverse bias kept in the range of 20 pA, while the forward bias increased rapidly. Upon the monochromatic light illumination (λ = 365 nm), the reverse photocurrent immediately increased, and approached to about 6 nA at bias of −2 V with a power density of 50 mW/cm^2, indicating a strong response to ultraviolet light. As seen from Figure 2d, the reverse photocurrent increases slightly with the power density upon light illumination with wavelength of 650 nm, indicating a relatively insensitive response to the light with this wavelength. Interestingly, it also deserves to note that the obvious photodiode-like, but not an ideal diode behavior, is observed in *n*-Si/*n*-MoS_2 heterostructures, where the reverse current increases by power density and tended to saturate, while the forward current keeps almost constant regardless of the power density[30]. The insets of Figure 2a–d present the enlarged areas near the zero point, where the slight short-circuit current (I_{sc}) and open-circuit voltage (V_{oc}) were observed. According to the band alignment at the interface between MoS_2 and *n*-Si (Figure 2e), the photodiode-like behavior can be understood as following. Firstly, from the point of the intrinsic nature of the electronic states of monolayer MoS_2, *ab* initio calculations of the density of states of monolayer MoS_2 shows strong peaks in the visible range, leading to the enhanced light absorption, as demonstrated by Britnell *et al*[19]. Upon light illumination with energy larger than the bandgap of monolayer MoS_2 (1.8 eV), the excitons from monolayer MoS_2 and *n*-Si were generated[19]. In the forward bias, the photoexcited holes in the valance band of MoS_2 could not move to *n*-Si due to the relatively larger barrier and lower band offset[31,32]. On the other hand, the photoexcited electrons at the conduction

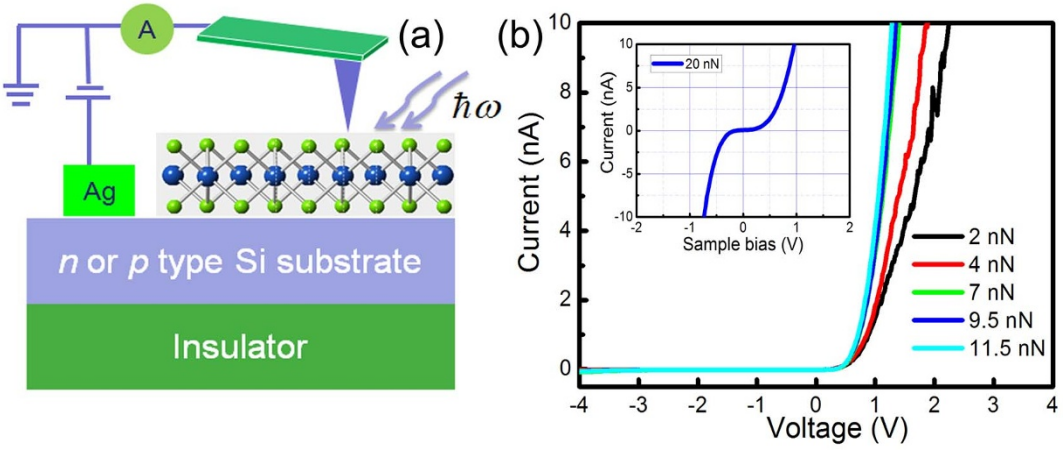

Figure 1 | (a) The schematic illustration of experimental setup of Si/MoS_2 heterostructures. Conductive AFM with Co/Cr tip was grounded and applied to measure the electrical behavior of Si/MoS_2 heterostructures upon light illumination with different light wavelengths and power densities. (b) The *I*–*V* curves dependent on the tip-sample contact force. The inset presents the *I*–*V* curve with larger contact force of 20 nN. The reverse bias increased rapidly, which may be resulted from the significant plastic deformation or even mechanical breakdown of monolayer MoS_2.

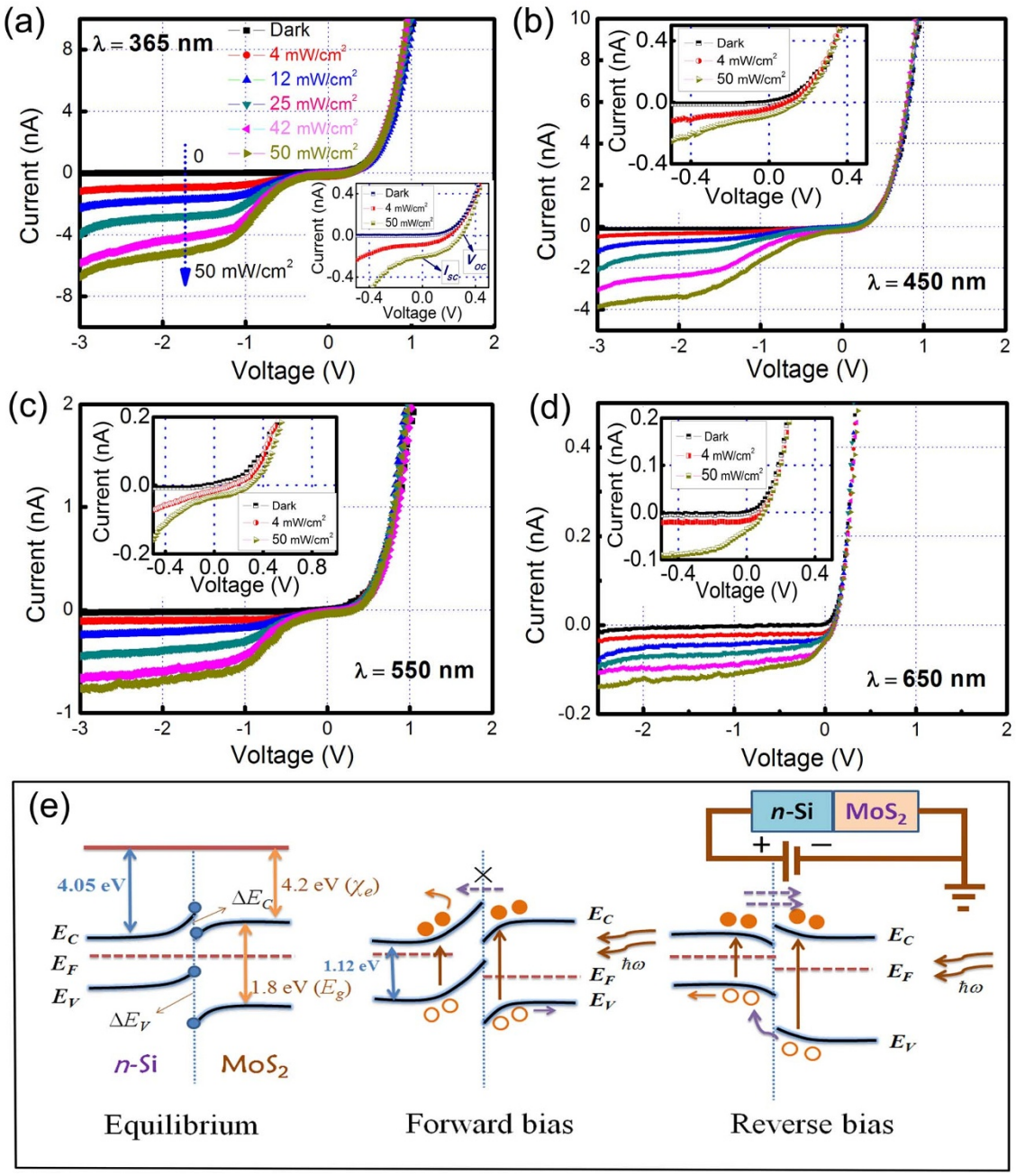

Figure 2 | *I–V* curves of *n*-Si/MoS_2 heterostructures upon light illumination of different wavelengthes: (a) 365 nm, (b) 450 nm, (c) 550 nm and (d) 650 nm. The power densities vary from 4 to 50 mW/cm². The *I–V* curves of *n*-Si/MoS_2 heterostructures present non-ideal photodiode-like behavior, where the reverse current increases with power density and the forward bias keeps almost constant regardless of power density. The weak photovoltaic effect was observed, where short current I_{SC} and open circuit voltage V_{OC} are small, as shown in insets of Figure 2a–d. (e) The band alignment at the interface between *n*-Si and monolayer MoS_2 at equilibrium, forward bias and reverse bias upon illumination. In the forward bias, photogenerated excitons could not be separated effectively due to the relatively larger barriers for holes and electrons transfer. However, the photogenerated holes could transferfrom the valance band of MoS_2 to *n*-Si, leading to the effective and efficient separation of excitons in the reverse bias.

band moved to the interface, forming an accumulated layer, and then recombined with holes at the valance band, leading to no efficient or sufficient separation of excitons in this case[33–35]. Therefore, the forward photocurrent had no net increase upon illumination. While, in the reverse bias, the large valance band bending facilitated the photoexcited holes transfer at the interface, resulting in the sufficient separation of excitons, and hence leading to the larger photocurrent. However, due to the smaller contact areas between the tip and MoS_2, the total number of separated photogenerated excitons was relatively smaller, leading to the weaker photovoltaic effect. Besides, considering that the bandgap of monolayer MoS_2 is about 1.8 eV and the corresponding critical exciting wavelength is about 680 nm, it is reasonable that compared with larger light wavelength, the lower light wavelength leads to larger photoexcited carriers, and thus the higher photocurrent is observed[10,23,24]. To further demonstrate the photoresponse behavior of the *n*-Si/MoS_2 heterostructures, we carried out photocurrent measurements with longer wavelengths higher than that of monolayer MoS_2 (680 nm). Interestingly, small photocurrent of about 14.2 pA at zero bias (I_{SC}) was observed upon illumination at light wavelengths of 710 nm with power density of 35 mW/cm², respectively; while there is no photocurrent generated at wavelength of 980 nm. (Figure S4, SI) These phenomena indicated

that both monolayer MoS_2 and *n*-Si took effects in the process of exticons generation[23,24]. Figure S6 also presents the dependence of photoresponsivity (R) on the power density at wavelengths of 710 and 808 nm, which is consistent with above analysis and band alignments in Figure 2e. In the supporting information, we also demonstrated the reproducibility of conductive AFM measurements, as shown in Figures S3 to S6.

Subsequently, we calculated the photocurrent and photoresponsivity of *n*-Si/monolayer MoS_2 heterostructure as a function of incident light wavelength and power density, and the results were shown in Figure 3. Figure 3a presents the dependence of photocurrent on the power density at different reverse biases. For lower reverse bias, the photocurrent increased nonlinearly with increasing the power density (See Figure 3a), while for higher reverse bias, the photocurrent was linear with power density. From Figure 3b, the photocurrent at reverse bias of −2 V shows a strong linear dependence on the light intensity from 4 to 50 mW/cm^2 for all four wavelengths, indicating a superior photocurrent capability. At wavelength of 650 nm, the photocurrent was rather small, and increased slightly. In contrast, the photocurrent with light illumination with 365 nm raised rapidly. We further calculated the photoresponsivity to evaluate the detection ability of *n*-Si/MoS_2 heterostructures. Photoresponsivity is defined as the photocurrent generated per unit power of the incident light on the effective area[10]. The photoresponsivity can be described using the following equation, $R = I_{ph}/(P \times S)$, where R is the photoresponsivity, I_{ph}, P, and S are the photocurrent, power density and illuminated area of Si/MoS_2 heterostructures (about 8 μm^2 for monolayer MoS_2 on *n*-Si substrate), respectively, we estimate the photoresponsivity as a function of wavelength and light intensity, as presented in Figure 3c and d[31]. R increased by decreasing the wavelength, while it decreased by increasing the power density, which may be caused by the large number of traps at the interface. Upon illumination, the density of effective photoinduced state decreased, leading to the decreased photoreponsivity when the power density increased. Since the shot noise from the dark current is the major contribution to the total noise in the photodetectors or photodiodes, the specific detectivity D^* is calculated by $D^* = RA^{1/2}/(2eI_d)^{1/2}$, where R is the photoresponsivity, A is the illuminated area of *n*-Si/MoS_2, and I_d is the dark current (less than 20 pA in our experiments)[11,33]. From Figure 3d, the calculated detectivity is dependent on the light wavelength, and it varied in the range of 10^9 Jones. This makes Si/MoS_2 heterostructures sensitive photodetectors in the photocurrent detection, and comparable to Si/graphene photodiodes (with D^* of 10^9 Jones)[33].

We also study the electrical properties of *p*-Si/monolayer MoS_2 upon illumination with light wavelength of 365 nm, and the results are presented in Figure 4. Figure 4a shows the I–V curves of *p*-Si/MoS_2 under light illumination with power density from 4 to 50 mW/cm^2. The I–V curve presents the rectifying characteristic without illumination, while the reverse bias increases immediately upon illumination, similar to the case of *n*-Si/MoS_2 heterostructures. The reverse photocurrent gradually increases with increasing the power density. Compared with *n*-Si/MoS_2 heterostructure, the photocurrent of *p*-Si/MoS_2 heterostructure increases slowly with power density, and tends not to saturate. The inset in Figure 4a presents the enlarged area near the zero point, and the I_{sc} and V_{oc} are clearly

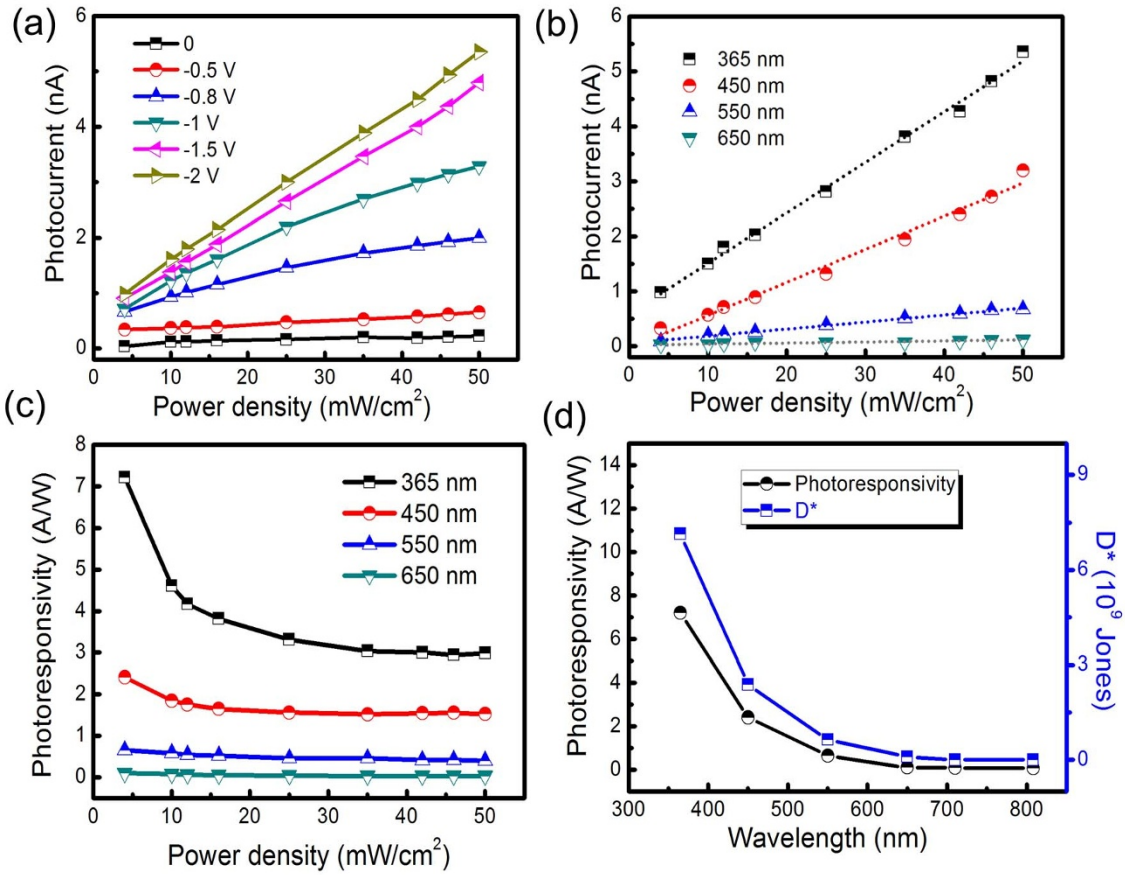

Figure 3 | Photoresponse property of *n*-Si/monolayer MoS_2 heterostructures. (a) Photocurrent as a function of power density for different applied bias for light illumination of 365 nm. (b) Photocurrent as a function of power density under light illumination with different light wavelength (365, 450, 550, and 650 nm). In spite of the variation of light wavelength, the photocurrent presents linear to power density. (c) The photoresponsivity as a function of power density under light illumination with different light wavelengths. The lower the power density, the higher the responsivity. (d) The photoresponsivity and the spectific detection as a function of light wavelength.

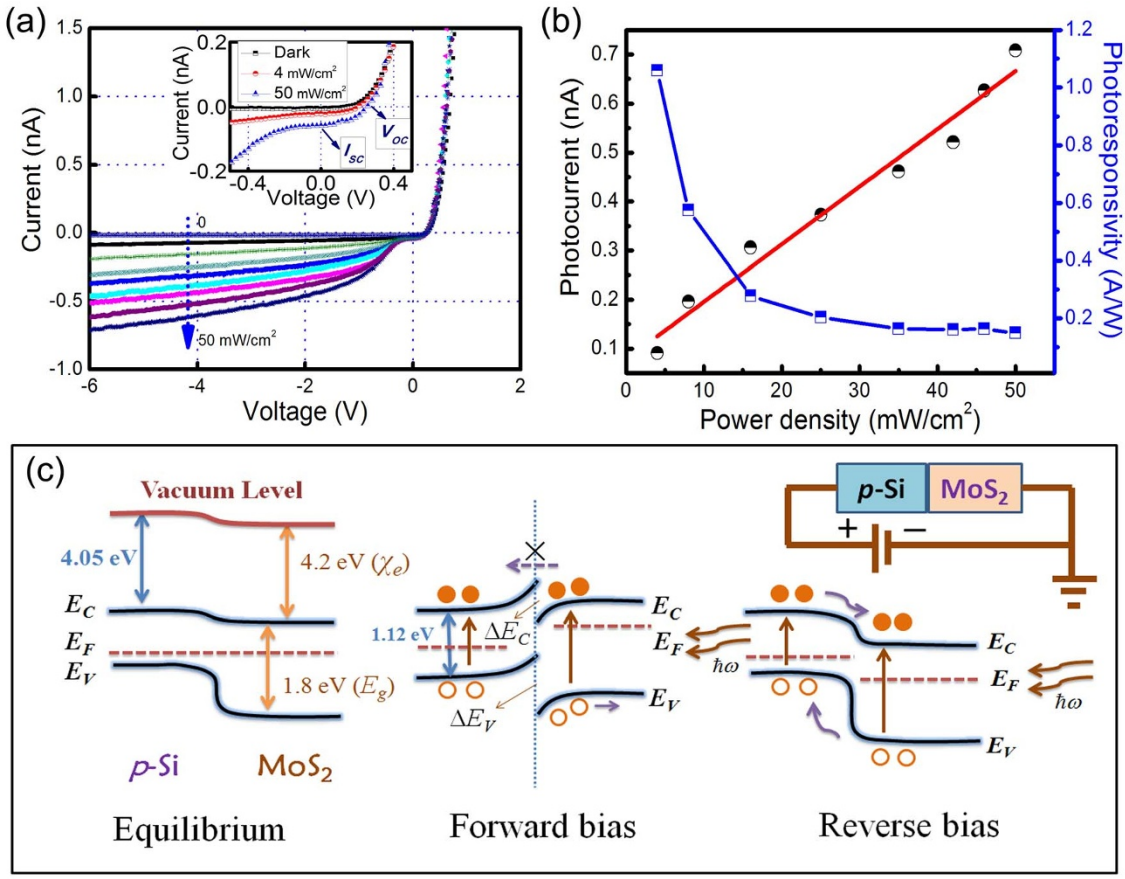

Figure 4 | The photoresponse property of *p*-Si/MoS_2 heterostructures. (a) The *I–V* curves of *p*-Si/MoS_2 heterostructures upon illumination with different power densities in a range of 4 to 50 mW/cm² with light wavelength of 365 nm. The reverse current increased by increasing power density, yet it did not saturate. (b) The photocurrent and responsivity as a function of power density at light wavelength of 365 nm. The photocurrent was linear with power density, while the responsivity decreased rapidly with power density. (c) The band alignment at the interface between *p*-Si and monolayer MoS_2 at equilibrium, forward bias and reverse bias upon illumination. Similar to the case of *n*-Si/MoS_2, the excitons in MoS_2 could be separated effectively at the interface in the reverse bias.

observed, which is smaller than that of *n*-Si/MoS_2 heterostructures. We also calculated the reverse photocurrent and photoresponsivity as a function of power density, as presented in Figure 4b. Compared with *n*-Si/MoS_2, the value of photocurrent and photoresponsivity were much smaller. From the point of band alignment at the interface (Figure 4c), *p*-Si/MoS_2 also belongs to typical type-II heterostructure[23,24,31,32]. In the forward bias, due to the upward bending of conductance band and downward bending of valance band, the photoexcited electrons and holes could not move towards *p*-Si side, resulting in the low-efficient separation of excitons[23,24,32]. Therefore, the forward current did not increase with illumination intensity. However, in the reverse bias, the large valance band offset of MoS_2 benefited to the transfer of photoexcited holes to *p*-Si, leading to the effective separation of excitons. Therefore, the reverse current increased with illumination. Compared with *n*-Si/MoS_2, the Fermi level difference of *p*-Si/MoS_2 is much smaller than that of *n*-Si/MoS_2, and the built-in electric field was too weak to separate photogenerated electron-hole pairs sufficiently and effeciently since the binding energy of photogenerated carriers is about 0.8–0.9 eV, leading to the lower photocurrent for *p*-Si/MoS_2 heterostructures[7,23,24].

Kelvin probe microscopy (KFM) has been proved to be a powerful tool to study charge separation and charge injection induced by the built-in electric field in photovoltaics[36–38]. The built-in potential is a fundamental characteristic of a material interface possessing a charge-separating junction, and it is a key component in photovoltaics to increase light-harvesting efficiency, which has been characterized by KFM[39]. It refers to the potential difference across the charge-depleted region at the junction, which is attributed to the equilibration of the Fermi level shift. In KFM, electrostatic force between the tip and sample results from a contact potential difference (CPD), which will be nullified by an applied DC bias[40]. Using Kelvin probe microscopy, the light-induced local surface potential change is mapped to demonstrate the proposed spatial charge separation mechanism at the interface of heterostructures.

Figure 5 shows the surface potential results without and upon illumination with light of 365 nm (power density is 10 mW/cm²). Figure 5a–c shows the topography and the corresponding potential maps of *n*-Si/monolayer MoS_2 heterostructures before and after illumination. It is interesting that unlike MoS_2 on SiO_2 substrate, where the surface potential of MoS_2 presents interlayer screening effects, MoS_2 on *n*- or *p*- silicon was significantly different from that on SiO_2 substrate. In Figure 5a, there were monolayer and bilayer MoS_2 on the *n*-silicon substrate, but the surface potential difference between monolayer and bilayer MoS_2 (Figure 5b) was not distinct[41–43]. (Figure S8, SI) Moreover, according to the evaluation of work function of *n*-Si and monolayer MoS_2 (about 4.3 and 4.9 eV, respectively), the surface potential difference was calculated to be about 0.6 V, inconsistent with the KFM results in our experiments, where the contact potential difference was about only 0.12 V. Although the absorbers on silicon or MoS_2 from external environment might have effects on the measurements of surface potential, it should not have such significant effect according to previous work[42,44]. Therefore, we conclude that there exists significant charge transfer process when Si and MoS_2 contact together. Upon illumination, the surface potential

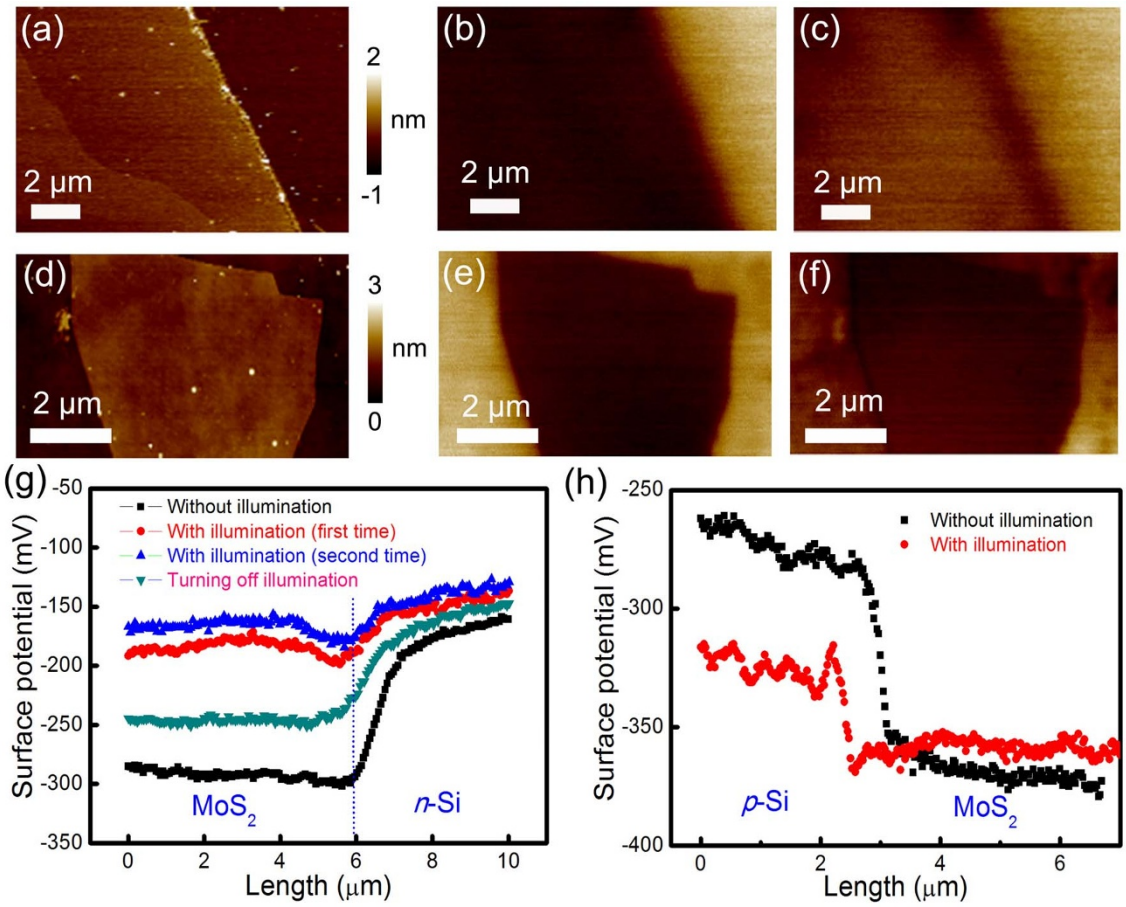

Figure 5 | The variation of surface potential of *n*- and *p*-Si/MoS_2 heterostructures without and upon illumination with light wavelength of 365 nm at power density of 10 mW/cm². (a)–(c) The topography and the corresponding surface potential maps of *n*-Si/MoS_2 heterostructures before and after illumination, respectively. (d)–(f) The topography and the corresponding surface potential maps of *p*-Si/MoS_2 heterostructures before and after illumination, respectively. (g) and (h) are the corresponding potential section profiles of *n*- and *p*-Si/MoS_2 heterostructures, respectively.

of *n*-Si and MoS_2 both increased, and the contact potential difference between *n*-Si and MoS_2 became smaller, as shown in Figure 5c.

However, in the case of *p*-Si/monolayer MoS_2 heterostructure, the surface potential of *p*-Si decreased, and that of MoS_2 increased slightly upon illumination, while the contact potential difference also decreased between *p*-Si and MoS_2. Subsequently, we quantitatively compared the variation of surface potential of *n*- and *p*-type Si/monolayer MoS_2, and the section profiles are presented in Figure 5g and h. In Figure 5g, the black and red lines present the section profile of surface potential mapping of *n*-Si/MoS_2 before and after illumination, respectively. It is observed that the surface potential difference of *n*-Si before and after illumination was less than 30 mV, while the counterpart of MoS_2 before and after illumination was larger than 120 mV. Moreover, under continuous illumination, the surface potential shifts towards larger value (for both *n*-silicon and MoS_2), indicating the increase of electron and accordingly a reduction of holes. This demonstrates the significant separation of photogenerated excitons. However, in the case of *p*-Si/MoS_2 heterostructures, the surface potential of Si decreased by 60 mV, while that of MoS_2 increased slightly upon illumination. These results demonstrated that the photogenerated excitons failed to significantly separate effectively due to the weak built-in electric field at the interface. Coupling KFM results with photoresponse measurement, we speculate that the built-in electric field for *n*-Si/MoS_2 is larger than the counterpart for *p*-Si/MoS_2 due to the difference of Fermi level shift. This built-in electric field difference can explain the slight reverse current increase upon illumination and the unsaturated reverse current for *p*-Si/MoS_2 heterostructures in Figure 4, where the smaller the built-in electric field, the slower the holes transfer.

Discussion

In order to reveal the origin of difference of photodiodes behaviors in *n*-Si/MoS_2 and *p*-Si/MoS_2 as clear as possible, we aim to explain it from the point of band alignments. It is easier to understand the photodiode behavior of *p*-Si/MoS_2 from the theory of p-n junctions, where the built-in electric field at the interface induces the separation of excitons[23,24,32]. According to the band alignments shown in Figure 4c, the excitons are separated efficiently, leading to the occurrence of photocurrent at zero bias. Since the minority carriers in p-n junction dominates the carrier transport, it will be beneficial for us to analyze the minority carrier transport in the forward and reverse bias[32]. In the reverse bias, both the valance and conductance band offset increases, the minority carriers (holes in MoS_2, and electrons in *p*-Si) have large potential to move under lower barriers, leading to the increase of reverse current. However, in the forward bias, due to the large barriers at the interface, the minority carriers have not enough driving force to surpass or tunnel the barriers, resulting in almost no variation of forward current[32].

In contrast to *p*-Si/MoS_2 (p-n junction), which is minority-carriers dominated device, *n*-Si/MoS_2 heterostructure (n-n junction) is different[32]. Due to the difference in electron affinity between the two materials, electrons are transferred from *n*-Si side to MoS_2 across the interface, and the resultant band bending leads to the formation of a barrier for electrons transport. From the *I*–*V* curves, the current

saturation under negative bias significantly deviated from the exponential current of p-n junction or a Schottky barrier[34,35]. This behavior is attributed to the dependence of the barrier height on applied voltage. Then, we will discuss the variation of band alignments and the charge transfer quantitatively in the forward and reverse bias upon illumination. In Figure 2e, under the applied reverse bias, an accumulation of photogenrated positive charges at the valance band gives rise to the narrowing and lowering of the barrier and thus enhances the tunneling of electrons through it[32]. Compared with p-n junction (p-Si/MoS_2), where the built-in electric field just is related to the intrinsic property of the two materials, the majority carriers transport in n-n junction (n-Si/MoS_2), and hence the photoresponsivity (and photogain) can be varied in a wide range by modulating the barrier height and width with the help of photogenerated excitons arriving at the vicinity of the interface[32,34,35]. In the forward bias, the barrier height and width enlarged, and electrons and holes can not tunnel from it, leading to the no variation of forward current.

In conclusion, we have verified photodiode-like behavior of (n- or p-type) silicon/monolayer MoS_2 heterostructures. The n-Si/MoS_2 heterostructures had excellent wavelength-dependent photodetection ability, and the photoresponsivity approached to about 7.2 A/W, while p-Si/MoS_2 heterostructures were relatively less sensitive to light illumination due to the weak built-in electric field at the interface. Meanwhile, the strong light absorption and the separation of photogenerated excitons were also demonstrated by KFM results before and after illumination. By comparing KFM results and band alignments of Si/MoS_2 heterojunctions, we also discussed the origin of photodiode-like behaviors, where it is attributed to the intrinsic built-in electric field in p-Si/MoS_2, and modulated barrier height (and width) in n-Si/MoS_2, respectively. Our work may benefit to the deep understanding of the integration of two-dimensional materials with more conventional three-dimensional semiconductors, and then improve the developments in the area of van der Waals heterostructures.

Methods

Transfer of monolayer MoS_2 onto Si substrates. Before transferring, the silicon substrates were seriously etched by HF solution in order to remove the pristine oxidized layers on the top surface. After identification of monolayer MoS_2 by Raman spectra, PL and AFM, monolayer MoS_2 was transferred to Si substrates using the transfer method described in Ref. 25.

Conductive AFM and the photoresponse measurement. Conductive AFM was tested by a scanning probe microscope (SPM, Bruker Dimension ICON-Pt) with conductive probes (Co/Cr coated tips). The current limit was set to be 10 nA, in order to improve the sensitivity and avoid possible electrical breakdown. By calculating the spring constant of the tip and the displacement, the effect of contact force on electrical curves was studied to obtain the reproducible results by eliminating some external factors, such as the wear of tips and the bad contact between the tips and MoS_2. The monochromatic light with different wavelengths (365, 450, 550, 650, 710, 808 and 980 nm) was applied, and the power density was calibrated by a power meter.

Surface potential of Si/MoS_2 heterostructures. Surface potential measurement of monolayer and multilayer MoS_2 was conducted by SPM (Bruker Dimension ICON-Pt) with conductive probes (Co/Cr and Pt/Ir coated tips). The working mechanism of KFM can been seen in previous reference[40]. For the measurement of surface potential, an a.c. amplitude of 900 mV and a liftheight of 60 nm were used.

Raman spectrometry. Raman spectroscope at the excitation wavelength of 532 nm was used. The laser beam was focused onto MoS2 samples by a 100× objective lens with an NA of 0.9. An integration time of 30 s and spectrometer at 1800 grooves/mm were used during the test.

1. Wilson, J. & Yoffe, A. The Transition Metal Dichalcogenides Discussion and Interpretation of the Observed Optical, Electrical and Structural Properties. *Adv. Phys.* **18**, 193–335 (1969).
2. Neto, A. C. Charge Density Wave, Superconductivity, and Anomalous Metallic Behavior in 2D Transition Metal Dichalcogenides. *Phys. Rev. Lett.* **86**, 4382 (2001).
3. Wang, Q. H., Kalantar-Zadeh, K., Kis, A., Coleman, J. N. & Strano, M. S. Electronics and Optoelectronics of Two-Dimensional Transition Metal Dichalcogenides. *Nat. Nanotechnol.* **7**, 699–712 (2012).
4. Jariwala, D., Sangwan, V. K., Lauhon, L. J., Marks, T. J. & Hersam, M. C. Emerging Device Applications for Semiconducting Two-Dimensional Transition Metal Dichalcogenides. *ACS Nano* **8**, 1102–1120 (2014).
5. Eda, G. & Maier, S. A. Two-Dimensional Crystals: Managing Light for Optoelectronics. *ACS Nano* **7**, 5660–5665 (2013).
6. Bernardi, M., Palummo, M. & Grossman, J. C. Extraordinary Sunlight Absorption and 1 nm-Thick Photovoltaics using Two-Dimensional Monolayer Materials. *Nano Lett.* **13**, 3664–3670 (2013).
7. Mak, K. F., Lee, C., Hone, J., Shan, J. & Heinz, T. F. Atomically Thin MoS_2: A New Direct-Gap Semiconductor. *Phys. Rev. Lett.* **105**, 136805 (2010).
8. Radisavljevic, B., Radenovic, A., Brivio, J., Giacometti, V. & Kis, A. Single-Layer MoS_2 Transistors. *Nat. Nanotechnol.* **6**, 147–150 (2011).
9. Podzorov, V., Gershenson, M., Kloc, C., Zeis, R. & Bucher, E. High-Mobility Field-Effect Transistors Based on Transition Metal Dichalcogenides. *Appl. Phys. Lett.* **84**, 3301–3303 (2004).
10. Yin, Z. *et al.* Single-Layer MoS_2 Phototransistors. *ACS Nano* **6**, 74–80 (2011).
11. Choi, W. *et al.* High-Detectivity Multilayer MoS_2 Phototransistors with Spectral Response from Ultraviolet to Infrared. *Adv. Mater.* **24**, 5832–5836 (2012).
12. Lee, H. S. *et al.* MoS_2 Nanosheet Phototransistors with Thickness-Modulated Optical Energy Gap. *Nano Lett.* **12**, 3695–3700 (2012).
13. Lopez-Sanchez, O., Lembke, D., Kayci, M., Radenovic, A. & Kis, A. Ultrasensitive Photodetectors Based on Monolayer MoS_2. *Nat. Nanotechnol.* **8**, 497–501 (2013).
14. Zhang, W. *et al.* High-Gain Phototransistors Based on a CVD MoS_2 Monolayer. *Adv. Mater.* **25**, 3456–3461 (2013).
15. Geim, A. & Grigorieva, I. Van der Waals Heterostructures. *Nature* **499**, 419–425 (2013).
16. Bertolazzi, S., Krasnozhon, D. & Kis, A. Nonvolatile Memory Cells Based on MoS_2/Graphene Heterostructures. *ACS Nano* **7**, 3246–3252 (2013).
17. Zhang, W. *et al.* Ultrahigh-Gain Phototransistors Based on Atomically Thin Graphene- MoS_2 Heterostructures. *Sci. Rep.* **4**, 3826 (2013).
18. Roy, K. *et al.* Graphene-MoS_2 Hybrid Structures for Multifunctional Photoresponsive Memory Devices. *Nat. Nanotechnol.* **8**, 826–830 (2013).
19. Britnell, L. *et al.* Strong Light-Matter Interactions in Heterostructures of Atomically Thin Films. *Science* **340**, 1311–1314 (2013).
20. Esmaeili-Rad, M. R. & Salahuddin, S. High Performance Molybdenum Disulfide Amorphous Silicon Heterojunction Photodetector. *Sci. Rep.* **3**, 2345 (2013).
21. Yu, W. J. *et al.* Highly Efficient Gate-Tunable Photocurrent Generation in Vertical Heterostructures of Layered Materials. *Nat. Nanotechnol.* **8**, 952–958 (2013).
22. Jariwala, D. *et al.* Gate-Tunable Carbon Nanotube-MoS_2 Heterojunction PN Diode. *Proc. Natl. Acad. Sci. USA* **110**, 18076–18080 (2013).
23. Lopez-Sanchez, O. *et al.* Light Generation and Harvesting in a van der Waals Heterostructure. *ACS Nano* **8**, 3042–3048 (2014).
24. Tsai, M.-L. *et al.* Monolayer MoS_2 Heterojunction Solar Cells. *ACS Nano* **8**, 8317–8322 (2014).
25. Dean, C. R. *et al.* Boron Nitride Substrates for High-Quality Graphene Electronics. *Nat. Nanotechnol.* **5**, 722–726 (2010).
26. Alaboson, J. M. *et al.* Conductive Atomic Force Microscope Nanopatterning of Epitaxial Graphene on SiC (0001) in Ambient Conditions. *Adv. Mater.* **23**, 2181–2184 (2011).
27. Lee, H., Lee, Y. K., Van, T. N. & Park, J. Y. Nanoscale Schottky Behavior of Au Islands on TiO_2 Probed with Conductive Atomic Force Microscopy. *Appl. Phys. Lett.* **103**, 173103 (2013).
28. Bertolazzi, S., Brivio, J. & Kis, A. Stretching and Breaking of Ultrathin MoS_2. *ACS Nano* **5**, 9703–9709 (2011).
29. Castellanos-Gomez, A. *et al.* Elastic Properties of Freely Suspended MoS_2 Nanosheets. *Adv. Mater.* **24**, 772–775 (2012).
30. Fraas, L. M. & Partain, L. D. *Solar Cells and Their Applications.* Wiley Press: 2010.
31. Alferov, Z. I. The History and Future of Semiconductor Heterostructures. *Semiconductors* **32**, 1–14 (1998).
32. Rhoderick, E. Metal-semiconductor contacts. *IEE Proceedings I (Solid-State and Electron Devices)* **129**, 1–14 (1982).
33. An, X., Liu, F., Jung, Y. J. & Kar, S. Tunable Graphene-Silicon Heterojunctions for Ultrasensitive Photodetection. *Nano Lett.* **13**, 909–916 (2013).
34. Sharabani, Y., Paltiel, Y., Sher, A., Raiman, A. & Zussman, A. GaSb/InAsSb heterostructure MWIR detector for high temperature operation. *Proc. SPIE* 6940 (2008).
35. Mikhailova, M. P. & Titkov, A. N. Type-II Heterojunctions in the Gainassb-Gasb System. *Semicond. Sci. Technol.* **9**, 1279–1295 (1994).
36. Chiesa, M. *et al.* Correlation between Surface Photovoltage and Blend Morphology in Polyfluorene-Based Photodiodes. *Nano Lett.* **5**, 559–563 (2005).
37. Luria, J. L. *et al.* Spectroscopic Imaging of Photopotentials and Photoinduced Potential Fluctuations in a Bulk Heterojunction Solar Cell Film. *ACS Nano* **6**, 9392–9401 (2012).
38. Spadafora, E. J., Demadrille, R., Ratier, B. & Grévin, B. Imaging the Carrier Photogeneration in Nanoscale Phase Segregated Organic Heterojunctions by Kelvin Probe Force Microscopy. *Nano Lett.* **10**, 3337–3342 (2010).
39. Nanayakkara, S. U. *et al.* Built-in Potential and Charge Distribution within Single Heterostructured Nanorods Measured by Scanning Kelvin Probe Microscopy. *Nano Lett.* **13**, 1278–1284 (2013).
40. Nonnenmacher, M., o'Boyle, M. & Wickramasinghe, H. Kelvin Probe Force Microscopy. *Appl. Phys. Lett.* **58**, 2921–2923 (1991).

41. Li, Y., Xu, C.-Y. & Zhen, L. Surface Potential and Interlayer Screening Effects of Few-Layer MoS_2 Nanoflakes. *Appl. Phys. Lett.* **102**, 143110 (2013).
42. Li, Y., Xu, C.-Y., Hu, P. & Zhen, L. Carrier Control of MoS_2 Nanoflakes by Functional Self-Assembled Monolayers. *ACS Nano* **7**, 7795–7804 (2013).
43. Castellanos-Gomez, A. *et al.* Electric-Field Screening in Atomically Thin Layers of MoS_2: the Role of Interlayer Coupling. *Adv.Mater.* **25**, 899–903 (2013).
44. Qiu, H. *et al.* Electrical Characterization of Back-Gated Bi-layer MoS_2 Field-Effect Transistors and the Effect of Ambient on Their Performances. *Appl. Phys. Lett.* **100**, 123104 (2012).

Acknowledgments

This work was supported by the National Basic Research Program of China (2012CB934102). C.X. acknowledges the support from the Fundamental Research Funds for the Central Universities (HIT.BRETIII.201203). The authors also thank Dr. Qingjiang Yu for discussion and Siqi Zhang for Raman spectra measurement.

Author contributions

Y.L., C.X. and L.Z. conceived and designed the experiments. Y.L. and J.W. performed the experiments. All authors discussed the results and contributed to the manuscript preparation.

Additional information

Supplementary information accompanies this paper at http://www.nature.com/scientificreports

Competing financial interests: The authors declare no competing financial interests.

How to cite this article: Li, Y., Xu, C.-Y., Wang, J.-Y. & Zhen, L. Photodiode-Like Behavior and Excellent Photoresponse of Vertical Si/Monolayer MoS_2 Heterostructures. *Sci. Rep.* **4**, 7186; DOI:10.1038/srep07186 (2014).